Large-Eddy Simulation of an open-channel flow bounded by a semi-dense rigid filamentous canopy: scaling and flow structure

A. Monti,[1] M. Omidyeganeh,[1] and A. Pinelli[1, a)]
City, University of London,
Northampton Square, London,
EC1V 0HB, UK

(Dated: March 12, 2019)

We have carried out a large-eddy simulation of a turbulent open-channel flow over a marginally dense, fully submerged, rigid canopy. The canopy is modelled as a set of unbendable, slender cylinders normally mounted on a solid wall. The flow in the canopy is resolved stem-by-stem by means of an immersed boundary method. It is found that the flow behaviour can be categorised according to the velocity distribution into two separate spatial regions: the canopy itself and the outer region above it. Within the region occupied by the canopy elements, the velocity magnitude is found to be related to the local shear stress. Outside the canopy, a logarithmic velocity profile matching the canonical turbulent open-channel flow over rough walls is recovered albeit the strong manipulation exerted by the canopy on the buffer layer. In the innermost layer, the presence of the stems is responsible for redistributing the local momentum fluctuations from a streamwise to a spanwise leading component, inhibiting the survival of the wall streamwise velocity streaks. On the other hand, the outer region presents a structure very similar to the well-known logarithmic boundary layer with the presence of large and energetic streamwise velocity streaks generated by a system of quasi-streamwise vortices. These vortices strongly contribute to the intra-canopy fluctuations through vigorous sweep and ejection events that affect all the region occupied by the stems. Consistently with the results of previous investigation[29,36], it is found that the inflection point in the mean velocity profile, produced by the drag discontinuity at the canopy tip, promotes the appearance of another system of spanwise oriented vorticity structures. However, differently from previous results reported in the literature[8], in our simulations the presence of alternating *head up - head down* hairpin vortices generated by a mutual induction of the counter-rotating spanwise vortices is not observed. Instead, we advocate that the modulation of the spanwise rollers is due to the action of the external logarithmic layer structures (i.e. the outer streamwise vortices that penetrate the canopy) rather than by upwash and downwash motions induced by the mutual interaction of the spanwise Stuart's rollers.

PACS numbers: 47.11.–j, 47.27.–i, 47.27.De, 47.55.dr
Keywords: canopy flow, roughness, large coherent structures, large-eddy simulation, immersed boundary method, scaling.

I. INTRODUCTION

Filamentous structures embedded in fluid flows are ubiquitous in nature performing several tasks. An interesting case is the one offered by vegetative plants in rivers (macrophytes) that significantly contribute in creating habitats for microorganisms by influencing the nutrient transport and deposition, by improving water quality (especially useful in the grey-waters treating) and by regulating the solar light up-taking[12,25,26,47]. Often, these flows are characterised by flow-plants interactions

a)Electronic mail: Alfredo.Pinelli.1@city.ac.uk.

able to trigger the development of large coherent flow structures that largely affect the scalar fluxes governing the nutrient exchange, sediment deposition, and the chemical reaction within the vegetative zones[28]. The environmental and possibly technological importance of turbulent flows over filamentous surfaces has driven a special interest in unravelling the mechanisms of the interaction between the vegetation and the flow. In particular, flows over in-stream-embedded vegetation have received much attention over the last decades. A pioneering study on canopy flows was carried out in 1949 by Ree and Palmer [38] that considered aquatic vegetated open-channel flows with the aim to determine their discharge capacity. In particular, the authors were interested in estimating the drag force exerted by the vegetation on the water stream. Following this early seminal research, the interest in these flows and the related publications grew constantly in time. Nowadays, the state-of-the-art research seems to suggest that untangling the physical behaviour of these flows can become an impossible task when the effects of all possible parameters are kept into account: vegetation distribution and density, macrophytes stiffness, level of submersion and Reynolds number just to mention few of them. More recent contributions focus on determining the effects of a few typical canopy parameters rather than consider a holistic scenario.

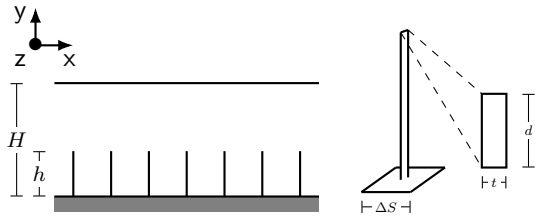

Figure 1: Basic geometrical parameters governing a canopy flow according to Nepf[29]. In the present configuration, the filaments are randomly distributed on the canopy bed, each one having been assigned an average area ΔS^2.

Along with this line, the research on aquatic plants, carried out by Nepf and co-workers[29] proposed to classify canopy flows only considering their geometrical properties. In particular, the ratio between the flow depth H and the canopy height h (i.e. the level of submersion, see Figure 1), was used to classify canopies as *emergent* ($H/h = 1$), *shallowly submerged* ($1 < H/h < 5$) and *deeply submerged* ($H/h > 10$). This classification allows separating canopy flows according to the relative importance between turbulent stresses, pressure gradient and drag forces[30]. For emergent canopies, the turbulence length scale is imposed either by the stem diameter d or by the average spacing between filaments ΔS if $\Delta S < d$ [29]. In emergent canopy flows, the momentum equation reduces to a balance between the drag force and the pressure gradient driving the mean flow. The consequence of this balance is the establishment of a self-similar velocity profile[22] which only depends on the ratio between the stems frontal area and the canopy area of influence $a(y) = d(y)/\Delta s^2$. In the submerged canopy condition, the flow approaches two limiting regimes[29,36], that are obtained when considering either very high or very low values of the canopy frontal solidity λ, defined as $\lambda = \int_0^h a(y)\,\mathrm{d}y$. In particular, if λ is much smaller than a threshold value (i.e. $\lambda \ll 0.1$, a condition termed *sparse* regime) then the flow velocity within and above the canopy shows an overall behaviour equivalent to the one observed in a turbulent boundary layer over a rough wall with a dominance of bed drag over the actual canopy form drag. Conversely, for large values of λ (i.e. $\lambda \gg 0.1$), the canopy drag becomes larger than the one offered by the bed. This condition, termed *dense* regime, is characterised by a drag profile discontinuity at the top of the canopy inducing the appearance of two inflection points in the mean velocity profile. One is located near the canopy edge while the second one lays by the canopy bed. As originally proposed by Belcher et al. [4], their presence leads to the generation of two separated shear layers. A more detailed characterisation of submerged canopy flows has been carried out by Poggi et al. [36] that undertook an experimental campaign on a set of rigid canopy flows by systematically varying the canopy stems density. The obtained results showed that the mean velocity profile has no or a weak inflection point at the canopy edge for values $\lambda < 0.04$

(sparse regime). Differently, in agreement with the classification given by Nepf[29], when $\lambda > 0.1$, the mean velocity profile features two pronounced inflection points. Motivated by their experimental observations, the authors also proposed two phenomenological models corresponding to the two extreme conditions. In the sparse regime, the flow is considered to behave like a boundary layer over a rough wall, while in dense regimes, the flow structure is envisaged to be a smooth composition of three different, dominant flow behaviours determined by the actual eddy size that can locally penetrate the canopy. In the inner region, i.e. $y/h \ll 1$, for sufficiently high Reynolds number the flow field is supposed to be characterised by the von Kármán street vortices, size and intensity depending on the diameter of the stems. The outer region, i.e. $y/h \gg 2$, would resemble a typical boundary layer over a rough wall, although in shallowly submerged canopies the development of the flow is constrained by the space available between the canopy edge and the free surface. In canopies characterised by a large H/h ratio ($H/h > 10$), a logarithmic boundary layer region is clearly observable[8,37]. Finally, in the space region by the canopy edge ($y/h \approx 1$), the flow is assumed to behave as a turbulent mixing-layer with an inflected mean velocity profile able to trigger a Kelvin-Helmholtz (KH) instability producing large scale spanwise rollers of a size comparable to the canopy height (the so-called *canopy-scale turbulence*)[29]. In the dense regime, these vortices would control the bulk momentum transport between the outer and the inner regions. Raupach and his collaborators[37] observed that in a fully developed mixing-layer, the streamwise wavelength of the initial KH instability, Λ_x, is preserved and moreover the ratio between Λ_x and the vorticity thickness of the mixing-layer, $\delta_\omega = \Delta U/(\partial U/\partial y)_{max}$ (where ΔU is the velocity difference between the low- and high-speed free-stream regions), falls into a specific range[8], $3.5 < \Lambda_x/\delta_\omega < 5$. These authors also suggest that in canopy flows, a direct comparison with the coherent structures appearing in canonical mixing layer flows can be inferred in the region close to the canopy edge. If the low-speed region velocity of the mixing layer is much lower than $U(h)$ (hypothesis verified if the canopy is very dense), the height of this region turns out to be proportional to the thickness of the vorticity layer developing at the canopy tip,

$$L_s = \frac{U(h)}{(\partial U/\partial y)_{(y=h)}} \approx \frac{1}{2}\delta_\omega. \qquad (1)$$

Raupach et al.[37] also observed that the ratio between the streamwise wavelength of the KH rollers and the shear scale (1) must fall into the range $7 < \Lambda_x/L_s < 10$. The validity of the former range was confirmed by several experiments over a wide range of canopies with different geometric properties. These experiments allowed to determine a more precise and robust relation given by $\Lambda_x = 8.1L_s$. Within the same context of dense, submerged canopies, Nezu and Sanjou[31] proposed a model sharing many features with the one proposed by Poggi and collaborators. In particular, they also postulated the existence of three regions characterised by different vorticity structures: the *emergent zone*, the *mixing-layer zone* and the *log-law zone*. These zones are not allowed to overlap significantly in space because the production mechanism of each zone would inhibit the growth of other vorticity structures[36].

Despite the amount of work done to unravel the physics of canopy flows, most of the knowledge accumulated until recent times was based on the limited information obtained from laboratory experiments[8,12,13,23,29,31,36,37] (usually 2D or point-wise measurements) and few numerical predictions based on simplified flow-vegetation interaction models[9,14,24]. Only recently, high-fidelity simulations have become a further research tool to be employed along with more classical approaches to study vegetative flows. Highly resolved simulations provide researchers with three-dimensional and detailed instantaneous flow representations. In particular, during the last decade, few large-eddy simulations (LES) of flows over dense canopies modelled by a system of volume forces[1,2,5,16,46], have demonstrated their capability of unravelling the intimate arrangement and the relation between the coherent structures above the vegetation layer. These new understanding also allowed to put forward conceptual models describ-

ing the generation and the evolution of the large scale coherent structures that ultimately determine the dominating features of canopy flows[1,2]. In this context, the recent simulations carried out by Bailey and Stoll[2] have shed some more light on the emergence and evolution of the coherent structures of a dense canopy flow. The authors found that near the canopy, quasi-two-dimensional mixing-layer-like rollers (reminiscent of those proposed by Raupach et al.[37]) dominate the transport of finer vorticity in and out of the canopy. In particular, the large, spanwise-oriented structures stretch upward forming hairpin shaped vortices that, in a later stage, break down generating a wider range of vorticity scales.

Although some pioneering numerical simulation has started to appear in the literature their application has been limited to dense canopy scenarios. These pioneering simulations did not resolve the canopy "stem-by-stem" by imposing the required zero-velocity boundary conditions on each element but rather relied on simulating the presence of the canopy using a distributed set of body forces mimicking the drag offered by the canopy on the flow. This approach can be considered to be physically sound for dense canopies but it would break down when applied to sparser canopies, where the hydrodynamic interactions between the stems become progressively important as the stem Reynolds number increases and local von Kármán wakes generate extra vorticity on the stem diameter scale. Moreover, the distributed drag approach fails to predict the drag close to the stems tips because the finite size of the filamentous elements is not kept into account in the local drag model.

Differently to other authors[43], the approach that we have considered in this work relies on a genuine direct simulation inside the canopy where a zero velocity boundary condition is imposed on every single stem. To our knowledge, this is the first simulation of a canopy flow offering such a high level of details. In particular, we report results obtained using an LES of a fully developed turbulent flow through an open-channel bounded by a shallowly submerged, mildly dense, rigid canopy layer. The aim of the work is to explore the mechanisms that govern the interaction between the turbulent flow and the canopy in a regime that, a priori, can be classified neither as dense nor as sparse. Identifying the proper scaling of a turbulent canopy flow in this regime is also one of our major motivations.

The paper is organised as follows. Section II describes the numerical method used to carry out the simulations including validation results and verification tests against more accurate but more expensive numerical methods. Section III provides descriptions and analyses of the obtained results, focusing on proper flow scaling and on the topology of the flow by characterising the shape and the evolution of the coherent turbulent structures embedded in the flow. Section IV outlines some conclusions, also providing a rationale for the use of resolved simulation in the framework of semi-dense and sparse canopies.

II. NUMERICAL METHOD

A turbulent flow over a rigid canopy has been simulated using an in-house developed incompressible Navier-Stokes solver (*SUSA*)[33]. In particular, we have adopted a large-eddy simulation (LES) approach where the governing equations are obtained by filtering out the velocity and pressure fluctuations taking place below a cut-off length scale chosen within the inertial range of turbulence. In a Cartesian frame of reference, indicating with x_1, x_2 and x_3 (u_1, u_2 and u_3) the streamwise, wall-normal and spanwise directions (the corresponding velocity components) the dimensionless incompressible LES equations for the resolved fields, $\overline{u}_i$ and $\overline{p}$, read as

$$\frac{\partial \overline{u}_i}{\partial t} + \overline{u}_j \frac{\partial \overline{u}_i}{\partial x_j} = -\frac{\partial \overline{P}}{\partial x_i} + \frac{1}{Re_b} \frac{\partial^2 \overline{u}_i}{\partial x_j \partial x_j} + \frac{\partial \tau_{ij}}{\partial x_j} + f_i, \qquad \frac{\partial \overline{u}_i}{\partial x_i} = 0. \tag{2}$$

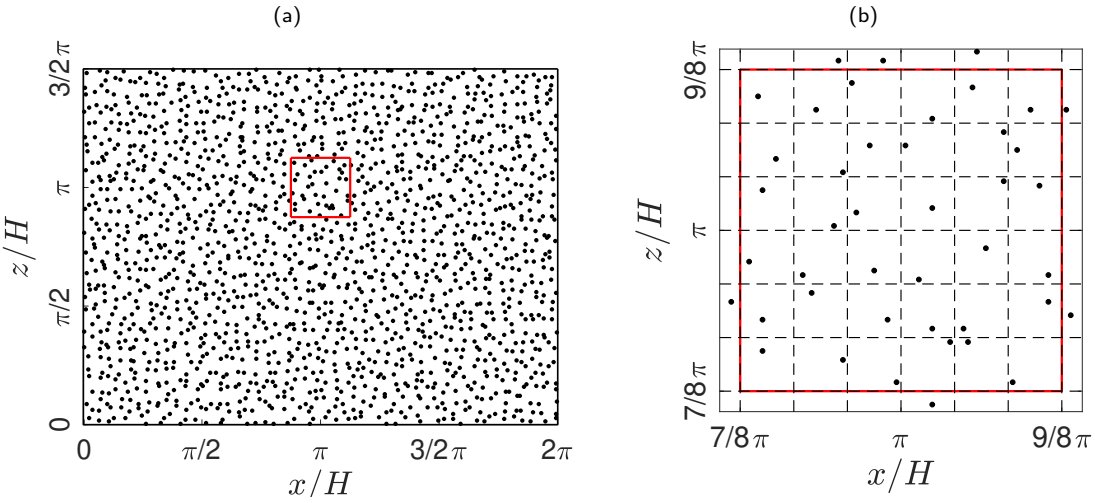

Figure 2: (a) Computational domain with the filaments distribution: wall-parallel view. The red box is zoomed out in (b), where the random allocation of each filament into its own tile of size $\Delta S \times \Delta S$ is highlighted.

In the given set (2), $Re_b = U_b H/\nu$ is the Reynolds number based on the bulk velocity U_b and the open-channel height H (being ν the kinematic viscosity) while $\tau_{ij} = \overline{u_i u_j} - \overline{u}_i \overline{u}_j$ is the subgrid Reynolds stress tensor[21]. The given set of equations requires the specification of a closure relating the subgrid, non-resolved stresses with the filtered, resolved field. In this work, we have adopted an eddy viscosity approach, where the former is evaluated using the Integral Length-Scale Approximation (ILSA) recently proposed by Rouhi et al.[41]. It is worth remarking that, within the canopy, the adopted subgrid model based on a "prefixed" turbulence integral scale switches off thus leading to a genuine direct numerical simulation between stems. Finally, note that in this paper the notation x, y, z and u, v, w is sometimes used to indicate space coordinates and velocity components.

The LES equations (2) are space discretised using a second-order accurate, cell-centred finite volume method. Pressure and velocity are co-located at the cell centre and the approach of Rhie and Chow[39] is used to avoid pressure oscillations. The equations are advanced in time by a second order semi-implicit fractional-step procedure[19], where the implicit Crank-Nicolson scheme is implemented for the wall-normal diffusive terms while an explicit Adams-Bashforth scheme is applied to the other terms. The Poisson pressure equation, that needs to be solved at each time step to enforce the solenoidal condition of the velocity field, is transformed into a series of two-dimensional Helmholtz equations in the wavenumber space via Fast Fourier Transform (FFT), along with the spanwise direction. Each of the resultant elliptic 2D problem is then solved using a preconditioned Krylov method (PETSc library[3]). In particular, we have found the iterative Biconjugate Gradient Stabilized (BiCGStab) method with an algebraic multigrid preconditioner (boomerAMG)[48] to behave quite efficiently. The code is parallelised using the domain decomposition technique implemented via the MPI message passing library. Further details on the code, its parallelisation and the extensive validation campaign, that has been carried out in other flow configurations, can be found in past work[32–34,40].

Unlike other approaches, we resolve each

canopy element by considering each stem as a rigid and solid filament with a finite cross-section perpendicularly flash mounted into the bottom wall. To enforce the boundary conditions that each rigid filament imposes on the fluid (i.e., zero velocity) we have used an immersed boundary (IB) method that deals with each stem using a set of distributed *Lagrangian* nodes that, in general, do not conform with the underlying finite volumes mesh. More specifically, the boundary conditions on the filaments are enforced using a set of distributed body forces defined on compact supports centred on each Lagrangian node that set to zero the fluid velocity at each time step[35]. The size of the support is related to the local grid size and also defines the hydrodynamic thickness of the filament (see previous studies[7,35] for more details). To distribute the stems within the canopy, we have subdivided the bottom wall in a mesh of uniform squares of area ΔS^2 (the *tiles*, see Figure 1). Each filament is then assigned to each elementary tile and mounted orthogonally to the wall in a randomly selected location within each square. The random assignment follows a uniform distribution allowing to minimise eventual channelling effects within the canopy, i.e. preferential flow corridors due to filaments alignment (see Figure 2). The tile size and the filament height h have been chosen to achieve a mildly dense canopy configuration. In particular, the frontal area solidity λ[29] has been set to $\lambda = 0.35$.

The canopy occupies the lower part of a computational box supposed to be periodic in the streamwise (i.e., x) and spanwise (i.e., z) directions. The size of the box in terms of the open-channel height H is set to $L_x = 2\pi$, $L_y = 1$ and $L_z = 3/2\pi$ (size similar to the one used by Bailey and Stoll[1] in their dense canopy simulation). The streamwise periodic condition stands on the assumption that the mixing layer developing at the edge of the canopy does not grow downstream as suggested by Ghisalberti and Nepf[13]. At the bottom wall, a zero velocity boundary condition is imposed while a free slip condition is enforced at the top surface. The whole domain is discretised with a Cartesian grid system with a number of nodes (equispaced in streamwise and spanwise directions) that yield a resolution in viscous units of $\Delta x^+_{in} \approx 3$, $\Delta y^+_{\mathrm{w},in} \approx 0.3$ and $\Delta z^+_{in} \approx 3$, in the streamwise, wall-normal and spanwise directions, respectively. The viscous units are defined in terms of the viscous length-scale at the bottom wall $\delta_\nu = \nu/u_\tau$, being $u_\tau = (\tau_\mathrm{w}/\rho)^{0.5}$ the friction velocity obtained from the wall shear stress at the bottom wall. Alternatively, one could define the viscous units in terms of the total shear stress on a plane parallel to the bottom wall, at a distance from the latter that depends on the virtual origin of the outer flow (to be defined in Section III). With this alternative definition, the resolution measured using the viscous units computed at the outer flow virtual origin turns out to be $\Delta x^+_{out} \approx 11$, $\Delta y^+_{\mathrm{vw},out} \approx 0.3$ and $\Delta z^+_{out} \approx 11$, thus within standard values for resolved LES of wall-bounded flows[20]. However, since the flow structure is not expected to resemble the one of a classical wall-bounded flow, a further assessment of the suitability of the numerical resolution within the canopy will be discussed in Section II B.

To maintain the channel equilibrium, a uniform pressure gradient is applied in the streamwise direction. In particular, at each time step, the pressure gradient is adjusted to conserve the flow rate. The resulting Reynolds number based on the bulk velocity and the domain height H has been fixed to $Re_b = 6000$, a value close to the one used in the experiments reported in[13]. The simulation parameters are summarized in Table I.

Table I: Simulation parameters.

	External units	Inner wall units	Outer wall units
Reynolds number	Re_b	$Re_{\tau,in}$	$Re_{\tau,out}$
	6000	270	940
Length	l/H	l^+_{in}	l^+_{out}
L_x	2π	1700	5900
L_y	1	270	940
L_z	1.5π	1270	4430
h	0.25	68	236
ΔS	0.131	35	133
Resolution	$\Delta l/\Delta S$	Δl^+_{in}	Δl^+_{out}
Δx	$1/12$	3	11
$\Delta y_{local,min}$	$1/120$	0.3	0.3
Δz	$1/12$	3	11

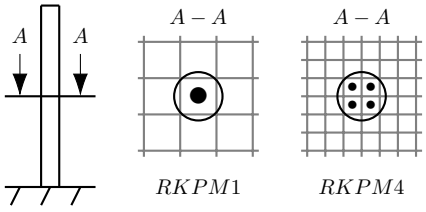

Figure 3: Filament cross section representation with RKPM method using one (RKPM1) or four (RKPM4) blobs.

A. IB method assessment

To verify the suitability of the method that we have used to enforce the zero velocity condition on the stems, we have carried out two sets of simulations on identical boxes (smaller than the one discussed in the previous section), with an identical driving force, using two distinct IB methods delivering different accuracies on the imposition of the boundary values on the immersed stems. One of the methods, the *reference case* adopts the bilinear direct forcing (DF) approach[6] that delivers a sharp zero velocity condition on the immersed body surface. Although quite accurate, this method requires a significantly higher resolution in the horizontal planes within the canopy than the alternative approach (RKPM) chosen for the present study. The variant of the *RKPM IB* method selected for the present study approximates each filament using a set of nodes distributed on a formally unidimensional stem. The effective thickness of the filaments depends on the size of the support containing the mesh nodes surrounding each stem node. Here we consider two types of support (see Figure 3), the first one (RKPM1) is made of a cage of three mesh nodes along each Cartesian direction, the second (RKPM2) is obtained as a union of four non-overlapping, neighbouring cages. On each elementary cage, we define a pseudo-Dirac delta function (a *blob*) that is used to enforce the boundary condition on each Lagrangian node used to discretise the stem[7]. Since the comparison between the three methods (DF vs RKPM1 vs RKPM4) is a purely numerical exercise, we have considered small computational boxes to avoid expensive calculations. In particular, we have considered a box built around a set of four filaments. The distribution of nodes along the vertical direction of each stem (i.e., the normal resolution) is kept uniform for all cases. The cross-plane resolution has been adapted to the requirements of the three IB methods as reported in Table II. The mean flow in all the simulation tests

Table II: Discretisation parameters used to compare the three IB methods

	DF	RKPM1	RKPM4
Re_b	≈ 6000	≈ 6000	≈ 6000
L_x/H	0.25	0.25	0.25
L_y/H	1	1	1
L_z/H	0.25	0.25	0.25
h/H	0.25	0.25	0.25
N_x	168	12	24
N_y	450	450	450
N_z	168	12	24

was driven by the same uniform pressure gradient chosen to be a periodic function of time mimicking a realistic turbulent condition obtained from a precursor simulation over a large computational box. Figure 4 shows that the three methods produce very similar mean velocity profiles. However, the Reynolds stresses inside the canopy differ considerably. In particular, considering the DF results as the baseline reference ones, the RKPM1 method is not sufficiently accurate (solid blue lines in Figure 4). On the other hand, the results achieved with the approximate RKPM4 approach reproduce satisfactorily higher order statistics within the canopy region. Apart from an accuracy assessment, the numerical tests also allow determining the equivalent size of the filament diameter obtained using an RKPM method. The latter does not define a sharp boundary surface but rather a set of mesh nodes where the boundary condition is only weakly enforced[7]. In particular, by comparing the drag obtained with the sharp DF method, we found that the effective diameter of a stem corresponds to $1.15\Delta x$, i.e. 1.15 times the linear size of the finite volume cell in the horizontal plane. Since the use of RKPM4, instead of the fully resolved DF approach, allows a massive saving in terms of

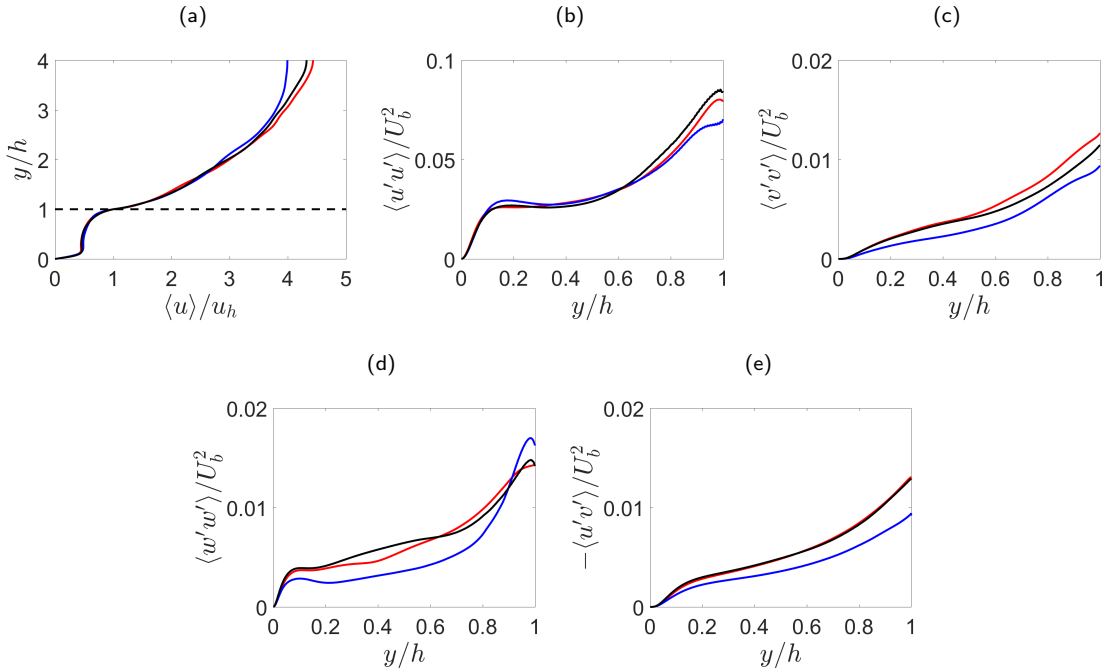

Figure 4: Comparison of the mean velocity and r.m.s. fluctuations profiles (only in the in-canopy region) obtained by using DF, RKPM1 and RKPM4 methods.Solid lines: red corresponds to DF, blue to RKPM1 and black to RKPM4. The dashed line in panel (a) is used to indicate the canopy edge (at height h.

required computational resources (at least two orders of magnitude in grid size), we have decided to undertake the set of realistic simulations using this method.

B. Validation case

While the baseline Navier-Stokes solver has been extensively validated in the past[32–34,40], its combination with a network of immersed filaments, modelled using the RKPM4 approach, required further validation. To this end, we have considered the flow over a submerged canopy that was experimentally characterised in the past by Shimizu et al.[44]. The parameters of the simulation used for the validation case are provided in Table III together with the corresponding experimental values[44]. The comparison of the mean velocity profile with the reference experimental data

Table III: Validation case parameters.

	Current	Ref.[44]
Re_b	7070	7070
$Re_{\tau,in}$	535	–
$Re_{\tau,out}$	1310	–
L_x/H	2π	–
L_y/H	1	1
L_z/H	1.5π	–
h/H	0.65	0.65
λ[29]	0.83	0.83
Resolution		
$\Delta x^+_{in} \times \Delta y^+_{\mathrm{w},in} \times \Delta z^+_{in}$	$6 \times 0.15 \times 6$	–
$\Delta x^+_{out} \times \Delta y^+_{\mathrm{h},out} \times \Delta z^+_{out}$	$20 \times 0.5 \times 20$	–

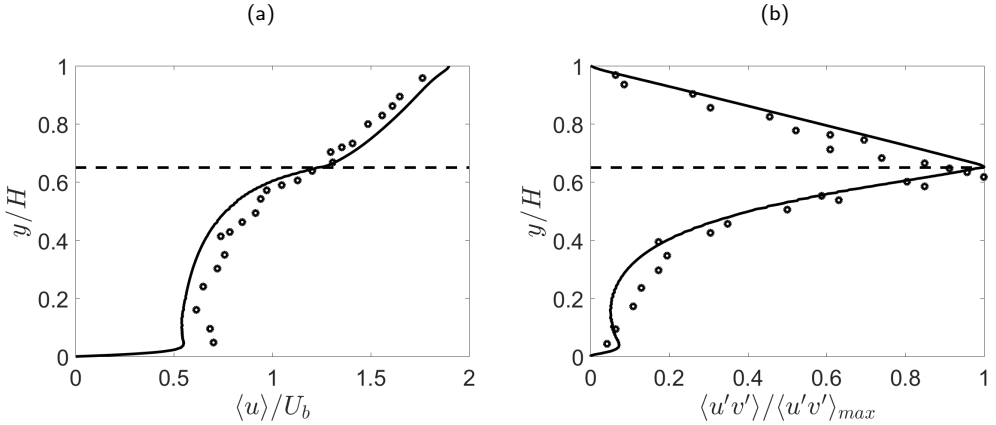

Figure 5: On the left, comparison of the predicted mean velocity profile (solid line) with the experimental values R31 of reference[44] (dotted curve). On the right, Reynolds shear-stress distribution predicted by the present numerical method (solid line) versus the experimental value R31[44]. The dashed line represents the location of the canopy tip at $y = h$.

reveals to be very good, as shown in the left panel of Figure 5. Even the Reynolds shear stress, plotted in the right panel of the same figure, shows a satisfactory agreement. Some minor inconsistencies can be observed in the velocity profile within the canopy that can be attributed to the limitations of the measurement technique in the region close to the solid elements.

III. RESULTS

As clearly visible from Figure 6 (a), the mean velocity profile of a turbulent canopy flow in a sufficiently dense regime (e.g., $\lambda > 0.1$[29]) exhibits two inflection points[29,36], one at the edge of the canopy and the other closer to the wall. The inflection points of the mean profile are ultimately caused by the drag exerted by the filamentous layer on the flow that produces a convexity in the velocity profile. The location of the inflection points can be evaluated by determining the zeros of the average momentum balance in the streamwise direction,

$$\frac{1}{Re_b}\frac{\partial^2\langle u\rangle}{\partial y^2} = \frac{\partial P}{\partial x} + \frac{\partial\langle u'v'\rangle}{\partial y} + \langle D\rangle. \qquad (3)$$

In the above, the symbol $\langle \cdot \rangle$ represents the triple average in time and in the two homogeneous spatial directions (i.e. x and z). In the balance equation (3), the first term represents the mean viscous force, the second is the mean pressure gradient, the third is the contribution of the mean Reynolds stresses and $\langle D\rangle$ contains the mean canopy drag. The two inflection points enclose a transitional zone between two boundary layers located in the innermost and outermost portions of the canopy[36] and can be thought of as a local Couette flow. Figure 6 (b) shows the mean velocity profile of the inner and the outer layers made dimensionless using two different friction velocities inside and outside the canopy. In particular, for the inner boundary layer, the friction velocity is defined as $u_{\tau,in} = \sqrt{\tau_w/\rho}$, being τ_w the skin friction at the bottom wall (i.e. $y/H = 0$). Differently, the external velocity profile is scaled with $u_{\tau,out}$, a velocity scale computed using the total shear stress evaluated at location y_{vo} within the canopy. In particular, y_{vo} is the origin of the external boundary layer assumed to obey the "shifted" velocity log-law,

$$\langle u\rangle = \frac{u_\tau}{\kappa}\log\left[\frac{(y-y_{vo})u_\tau}{\nu}\right] + B, \qquad (4)$$

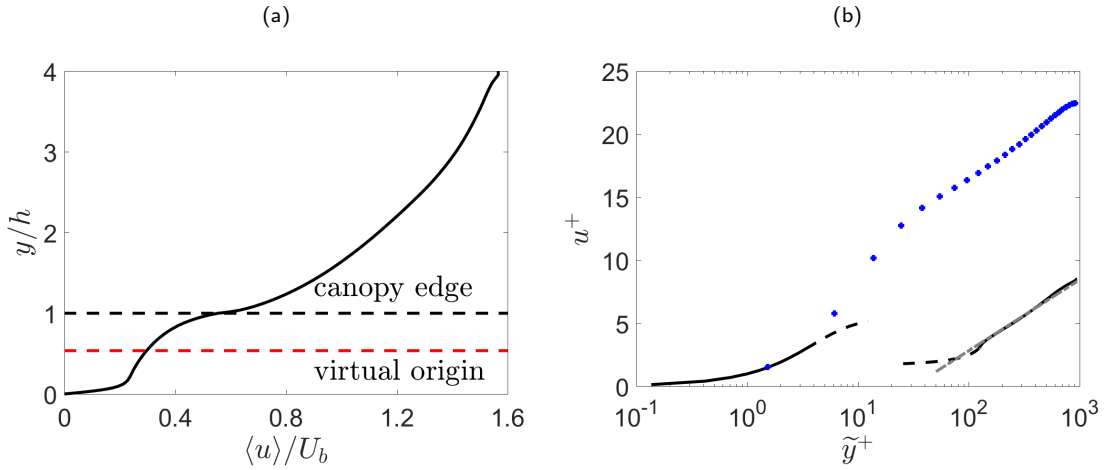

Figure 6: Mean velocity profiles. On the left, the velocity profile normalized with the outer units. The black dashed line represents the canopy height at $y = h$. The red dashed line identifies the position of the virtual origin of the outer region. On the right, the blue dotted line shows the velocity profile of a smooth wall channel flow at $Re_\tau = 950$[15]. The black line represents the results of the present simulation scaled with the inner and the outer wall units.

where $u_\tau = u_\tau(y_{vo})$. Equation (4) is a nonlinear, implicit equation that can be used to determine the value of y_{vo} for any given value of κ. For the present configuration and imposing the canonical value $\kappa = 0.41$, the virtual origin turns out to be located at $y_{vo}/h = 0.55$, as indicated in Figure 6 (a) with a dashed red line. Concerning the inner flow, Figure 6 (b) reveals that the flow matches a typical velocity profile of a turbulent channel flow only in the viscous sub-layer, where the wall skin friction drag dominates the drag of the stems. As it will be further discussed, it is also noticed that the buffer layer profile is completely altered by the combined actions of the stems-induced hydrodynamics and by the penetration of the outer flow. Differently, when scaling the outer flow velocity profile with the friction velocity computed at the virtual origin, a standard boundary layer logarithmic profile is recovered. As expected, the intercept B in equation (4) differs from the usual value of a flow over a smooth wall, indicating that the canopy layer behaves like a rough surface as seen by the outer flow[17]. Although the standard buffer layer characteristics are altered by the presence of the stems, overall the logarithmic structures of the outer flow are not drastically modified. In different frameworks, the unaltered and robust behaviour of the outer large scale motions in the logarithmic layer, when the region close to the wall (i.e. the buffer layer) is artificially manipulated, have also been reported by other authors[10,27]. In particular, Flores and Jiménez[10] have carried out numerical experiments replacing the smooth-wall boundary condition with imposed velocity disturbances, while Mizuno and Jiménez[27] have completely removed the wall imposing instead a condition based on matching a prescribed buffer layer turbulent velocity profile, typical of flows over rough surfaces. Both numerical experiments showed a very robust and consistent behaviour of the outer flow structure. Next, we consider the average momentum balance (3) integrated from the wall to a distance

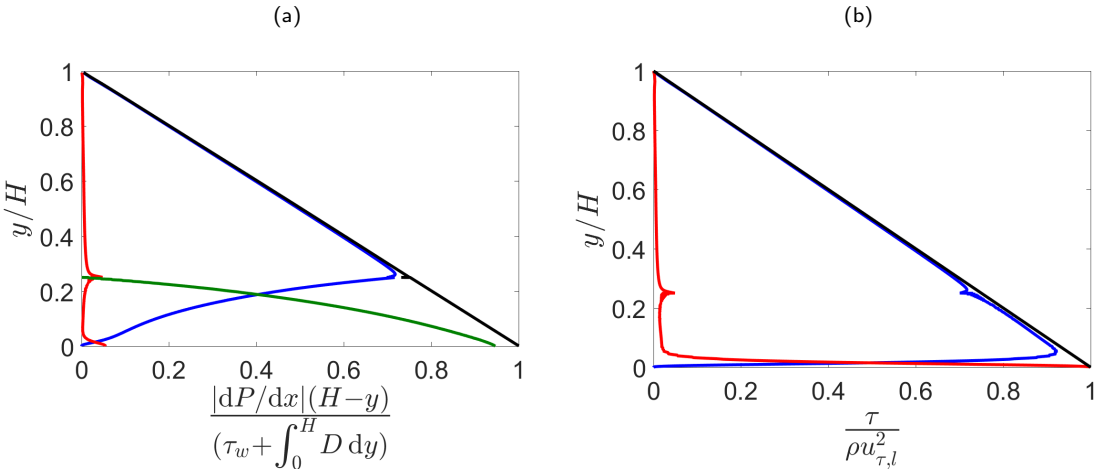

Figure 7: Pressure gradient balance. a) The black line represents the left hand side of the equation (5), the red line is the viscous shear stress, the blue line is the Reynolds shear stress and the green is the cumulative drag component. b) The viscous and the Reynolds shear stresses have been rescaled with the local friction velocity (10)

.

y measured from the bed location,

$$\frac{\partial P}{\partial x}y + \tau_w + \int_0^H \langle D\rangle \,\mathrm{d}y = \mu\frac{\partial\langle u\rangle}{\partial y} - \rho\langle u'v'\rangle + \\ + \int_y^H \langle D\rangle \,\mathrm{d}y. \quad (5)$$

Integrating equation (3) again, using as an upper limit of the integral the free-shear surface location, i.e. substituting $y = H$ in equation (5), the total balance (5) reads as

$$\tau_w + \int_0^H \langle D\rangle \,\mathrm{d}y = -H\frac{\partial P}{\partial x}. \quad (6)$$

Therefore, equation (5) can be also restated as

$$\left(1-\frac{y}{H}\right)\left|\frac{\partial P}{\partial x}\right|H = \mu\frac{\partial\langle u\rangle}{\partial y} - \rho\langle u'v'\rangle + \\ + \int_y^H \langle D\rangle dy. \quad (7)$$

The computed contributions of all the terms appearing in the balance are reported in Figure 7 (a). To include the contribution of the mean drag into the shear stress, we can reorganise equation (7), thus obtaining

$$\mu\frac{\partial\langle u\rangle}{\partial y} - \rho\langle u'v'\rangle = \left(1-\frac{y}{H}\right)\left|\frac{\partial P}{\partial x}\right|H + \\ - \int_y^H \langle D\rangle \,\mathrm{d}y = f(y)\left(1-\frac{y}{H}\right)\left|\frac{\partial P}{\partial x}\right|H, \quad (8)$$

where $f(y)$ is a dimensionless shape function defined as

$$f(y) = 1 - \frac{\int_y^H \langle D\rangle \,\mathrm{d}y}{\left(1-\frac{y}{H}\right)\left|\frac{\partial P}{\partial x}\right|H}. \quad (9)$$

From the balance of equation (8), it is possible to introduce a local friction velocity[45] that incorporates the contribution of the mean drag in the

total stress,

$$u_{\tau,l}(y) = \sqrt{\frac{f(y)}{\rho}\left|\frac{\partial P}{\partial x}\right|H} = \\ = \sqrt{\frac{\mu\partial_y\langle u\rangle - \rho\langle u'v'\rangle}{\rho(1-y/H)}}. \quad (10)$$

It is easy to verify that, when the total stress is scaled by $u_{\tau,l}(y)$, the non-dimensional linear profile $(1-y/H)$ is recovered as shown in Figure 7 (b).

Figure 8 shows the diagonal Reynolds stresses outside and inside the canopy, with a standard and a local, i.e. (10), normalisation. Outside the canopy, the velocity fluctuations reveal a clear resemblance with the ones in an open-channel flow over a rough surface, as for example reported by Scotti[42]. The behaviour of the diagonal stresses outside the canopy highlights once more that, away from the wall, surface roughness or even filamentous canopy elements have little effects on the structures of the external flow. In Figure 8, we also compare the normal Reynolds stresses distribution made non-dimensional with both the local friction velocity, as in (10) and with the outer friction velocity $u_{\tau,out} = u_\tau(y_{vo})$. The figure also displays how the canopy influences the velocity fluctuations in the wall-parallel directions, weakening the streamwise component, while significantly increasing the intensity of the spanwise fluctuations. This redistribution of velocity fluctuations is generated by the presence of the stems that disrupt the coherence of the streamwise velocity fluctuations while acting as obstacles that continuously deviates the flow in the spanwise direction. This mechanism is confirmed by the distribution of the vertical component of the velocity fluctuations that remain almost unaffected by the blocking effect of the obstacles, showing the "bi-dimensional" effect of the stems in the innermost region of the canopy. From Figure 8 one can also assess the range of validity of the proposed scaling (10) that breaks down as the canopy edge is approached. A possible explanation of this deficiency can be based on the unbalance between turbulence production and dissipation as already

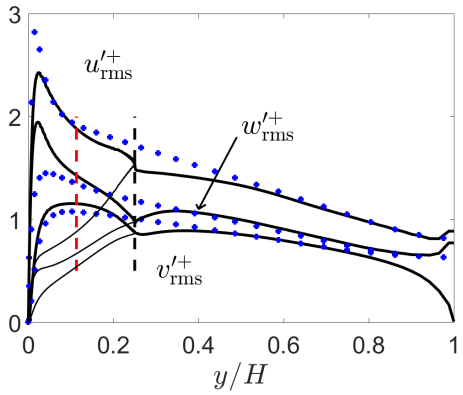

Figure 8: Velocity fluctuations RMS. Comparison between the present case (solid black) normalised with the local friction velocity $u_{\tau,l}$ (thicker line) and the reference values from the turbulent channel flow at $Re_\tau = 950$[15] (blue dotted). The difference in v'^{+} at the top of the domain is due to the different boundary conditions (open-channel vs. channel flow) applied for the simulation. The thin black solid line represents the RMS of the velocity fluctuations normalised with the outer friction velocity $u_{\tau,out}$ evaluated at y_{vo}. The black and red dashed lines refer to the same locations as in Figure 6.

suggested for flows with an imposed, discontinuous body force by Tuerke and Jiménez[45]. From Figure 9, we notice a production peak close to the bed that, differently from a standard channel flow, drops soon after having reached its maximum value. A second broader peak is also present just outside the canopy region. This external maximum suggests that the outer flow is possibly extracting energy from the canopy region.

Another interesting observation concerns the peaks of the velocity fluctuations which locations match the ones of the reference channel flow[15] albeit fully embedded within the canopy. From Figure 10, displaying the profiles of the vorticity fluctuations, it is noticed that the location of the peak of the wall-normal component $\omega_{y,rms}$ is only slightly shifted outwards when compared to the set of channel flow reference data[15]. The short distance between the peaks further emphasises the

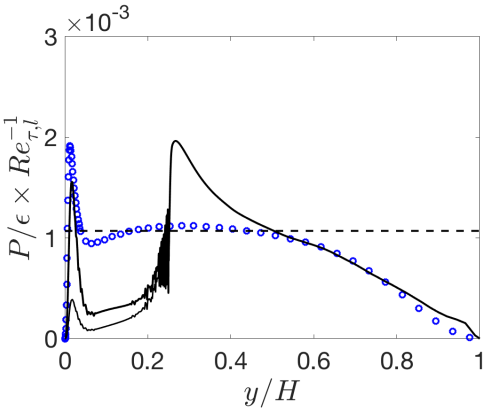

Figure 9: Turbulent kinetic energy production normalised with the dissipation and the local friction Reynolds number, defined as $Re_{\tau,l} = u_{\tau,l}H/\nu$, where $u_{\tau,l}$ is as in (10). The thinner black solid line is the same quantity normalised with the outer friction Reynolds number. The dashed line represents the equilibrium between the production and the dissipation of the turbulent kinetic energy, $1/Re_{\tau,l}$.

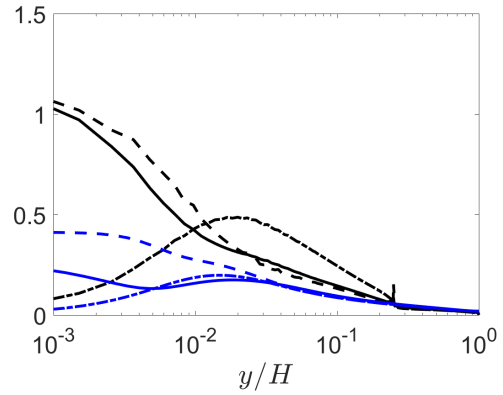

Figure 10: Black lines refer to the actual canopy simulation while the blue ones are taken from the channel flow data of Hoyas and Jiménez [15]. Solid line $\omega'^{+}_{x,rms}$, dashed-dotted line $\omega'^{+}_{y,rms}$, dashed line $\omega'^{+}_{z,rms}$. The wall units are based on the local friction velocity $u_{\tau,l}$.

analogy between the outer region of the canopy flow with the flow developing over a rough wall. This shift between peaks can be attributed to the variation of the spanwise velocity fluctuation in the streamwise direction (i.e. $\partial w/\partial x$) caused by the presence of the filamentous canopy. The instantaneous snapshots in Figure 11, representing the velocity fluctuations on a plane parallel to the bed within the canopy, clearly illustrates the effect of the stems that deviate the flow in a sinuous fashion in the spanwise and streamwise directions contributing to the increase of the coherence of the spanwise velocity fluctuations w'.

Further insight on the emergence and on the organisation of the large coherent structures that characterise the flow can be obtained by considering the spectral energy content and the two-point velocity autocorrelation function of the velocity components. The top row of Figure 12 and of Figure 13 shows the premultiplied spectra and the two-point autocorrelation functions of the velocity fluctuations as a function of the distance from the bed and as a function of either wavelengths λ_x or the streamwise separation Δx. Figure 12 was obtained by averaging the spectra of the velocity fluctuations in the spanwise direction, while Figure 13 was obtained by pre-applying the spanwise average operator, $\langle \cdot \rangle_z$, to the velocity fluctuations and then computing the two-point autocorrelation function in the streamwise direction. As an example, the autocorrelation function in the streamwise direction of the pre-averaged u component, $\langle u' \rangle_z$, can be computed as

$$R_{u'u'} = \frac{\langle \, \langle u' \rangle_z(0,y) \, \langle u' \rangle_z(\Delta x, y) \, \rangle}{\langle u' \rangle_z^2(0,y)}. \qquad (11)$$

This technique is useful to highlight the larger structures that populate the flow. The second row of the same two figures report the same quantities, averaged (or pre-applying the streamwise averaged operator, $\langle \cdot \rangle_x$, to the velocity fluctuations, as described above) in the streamwise direction as a function of either the spanwise wavelength λ_z or the separation Δz. A quick glance at Figure 12 reveals the presence of fluctuations maxima taking place within three spatial strips separated along the wall-normal direction. Some extrema

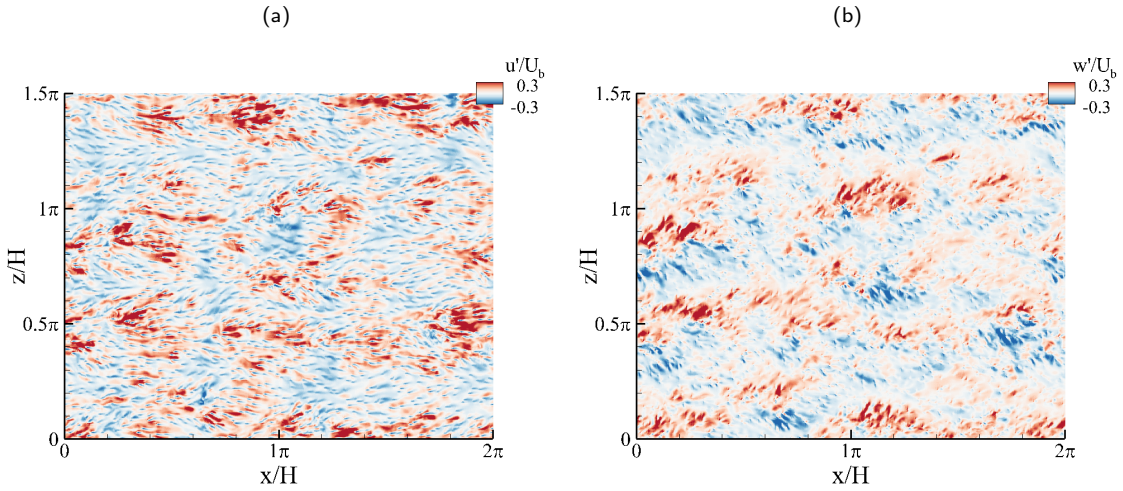

Figure 11: Instantaneous contours of streamwise (a) and spanwise (b) velocity fluctuations inside the canopy, on a plane located at $y/H = 0.02$.

are localised in the outer region, while others lie within the canopy either in its core or in the bed proximity. With the aim of simplifying the interpretation of the spectra, we also consider Figure 14 illustrating the same premultiplied spectra as a function of the stream- and spanwise wavelengths at three wall-normal locations roughly corresponding to the centres of the three aforementioned regions (no space average involved). Concerning the outer region, panel (g) in Figure 14 and panel (a) of Figure 12 and 13 reveal the presence of highly elongated streamwise velocity streaks that span a third of the domain in the spanwise direction (panel (d) of Figure 13). The large outer velocity streaks are also clearly visible in the instantaneous snapshot of Figure 15. The v' and w' energy maxima located just above the canopy displayed in panels (b) and (c) of Figure 12 show that the outer velocity streaks are connected with a system of streamwise vortices with an average streamwise length of roughly one channel height H, separated by about the same distance $\lambda_z \simeq H$ in the spanwise direction (see panels (h) and (i) of Figure 14). The streaklines obtained by space averaging the v and w component using a time snapshot plotted on the y-z side of the computational box in Figure 15, offer clear visual evidence of the presence of these streamwise vortices that penetrate vertically the whole canopy (see panels (d), (e) and (f) of Figure 13 as well). The existence of streamwise coherent velocity streaks above the canopy has been reported in previous studies[2,9]. They also highlighted the co-existence of the outer velocity streaks with large hairpin vortices whose heads are sequentially pointing upward and downward. On one hand, our results seem to confirm that the outer flow is characterised by the typical structure found in the logarithmic region of wall-bounded flows. The latter is known not to be very much affected by the geometric details of the solid boundary, presenting an almost universal behaviour[10,27]. On the other hand, we were not able to clearly evince the presence of the aforementioned hairpin vortices, whose full appearance could have been inhibited by the constraining effect of the channel height that would limit our observation to their legs, eventually shaped as vortices elongated in the streamwise direction.

The energy distribution in the region occupied by the core of the canopy is shown in the central row of Figure 14 that reveals a bimodal pattern. While the footprints of the outer structures are

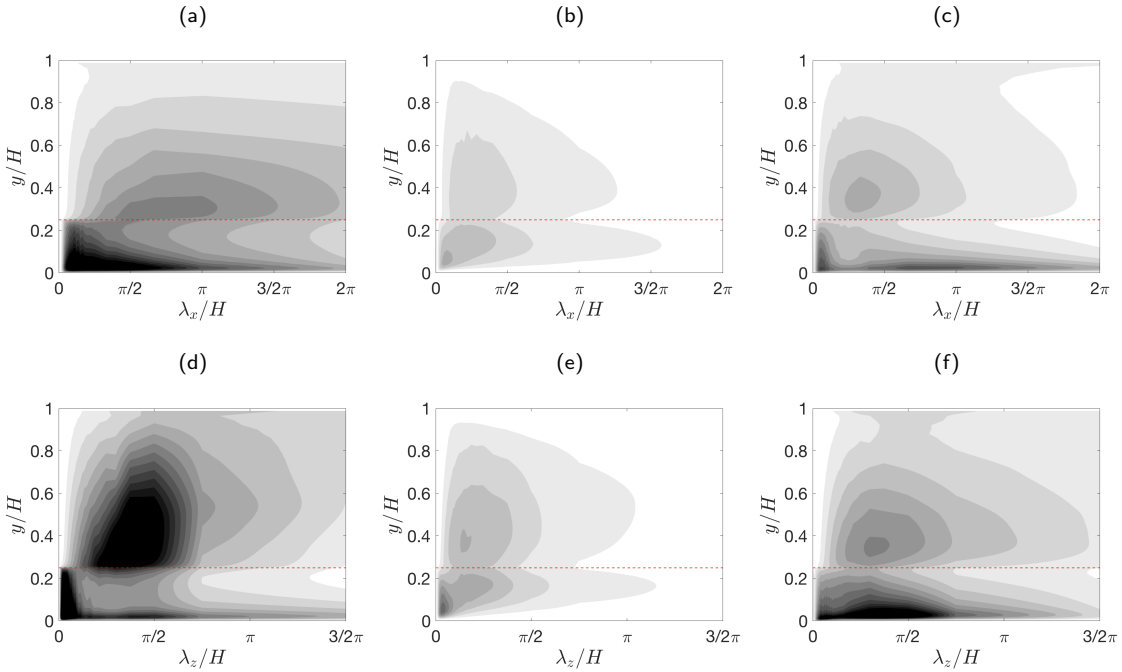

Figure 12: (a) Premultiplied spectra $\kappa_x \Phi_{u'u'}/u^2_{\tau,l}$. (b) Premultiplied spectra $\kappa_x \Phi_{v'v'}/u^2_{\tau,l}$. (c) Premultiplied spectra $\kappa_x \Phi_{w'w'}/u^2_{\tau,l}$. (d) Premultiplied spectra $\kappa_z \Phi_{u'u'}/u^2_{\tau,l}$. (e) Premultiplied spectra $\kappa_z \Phi_{v'v'}/u^2_{\tau,l}$. (f) Premultiplied spectra $\kappa_z \Phi_{w'w'}/u^2_{\tau,l}$. The levels range from 0 (white) to 0.6 (dark) with spacing of 0.05. The red dashed line represents the canopy height. All the spectra are normalised with the local friction velocity. The wavelengths, instead, are normalised with the flow depth.

still visible for all velocity fluctuations (i.e. peaks at $\lambda_x/H = \lambda_z/H = \mathcal{O}(1)$ for v' and w', and $\lambda_x/H \sim 2-3$, $\lambda_z/H = \mathcal{O}(1)$ for u'), a set of new maxima is generated for shorter wavelengths. While the peak of w' seems to be inherited from the outer vortices that penetrate the canopy (see also panel (f) of Figure 13), the peak of u' in panel (d) of Figure 14 that penetrates down to the canopy bed (see panel (a) of the same figure) is related to the appearance of a system of spanwise oriented vortices. This observation is confirmed by two-point velocity autocorrelation functions, especially the one that concerns the normal-to-the-wall component that is less affected by the filtering effect of the canopy stems. Indeed, panel (b) of Figure 13 shows that, inside the canopy, the v' correlation goes from positive to negative values within a streamwise correlation length of roughly one canopy height that matches the one corresponding to maximum of the energy content of v' (i.e. the location of the internal maxima in panel (e) of Figure 14). This system of vortices is not easily detectable from the streamwise two-point autocorrelation of u' partly because of the disrupting effect of the canopy elements and partly because modulated in the spanwise direction by the presence of the outer structures: note that the spanwise correlation length of u' in panel (d) of Figure 13 matches the ones of panels (e) and (f) in the same row of the same figure. Nonetheless, the existence of organised short spanwise rollers is confirmed by visual inspection of the streaklines plotted on the y-x side of the computational box in Figure 15 (streaklines obtained by spanwise av-

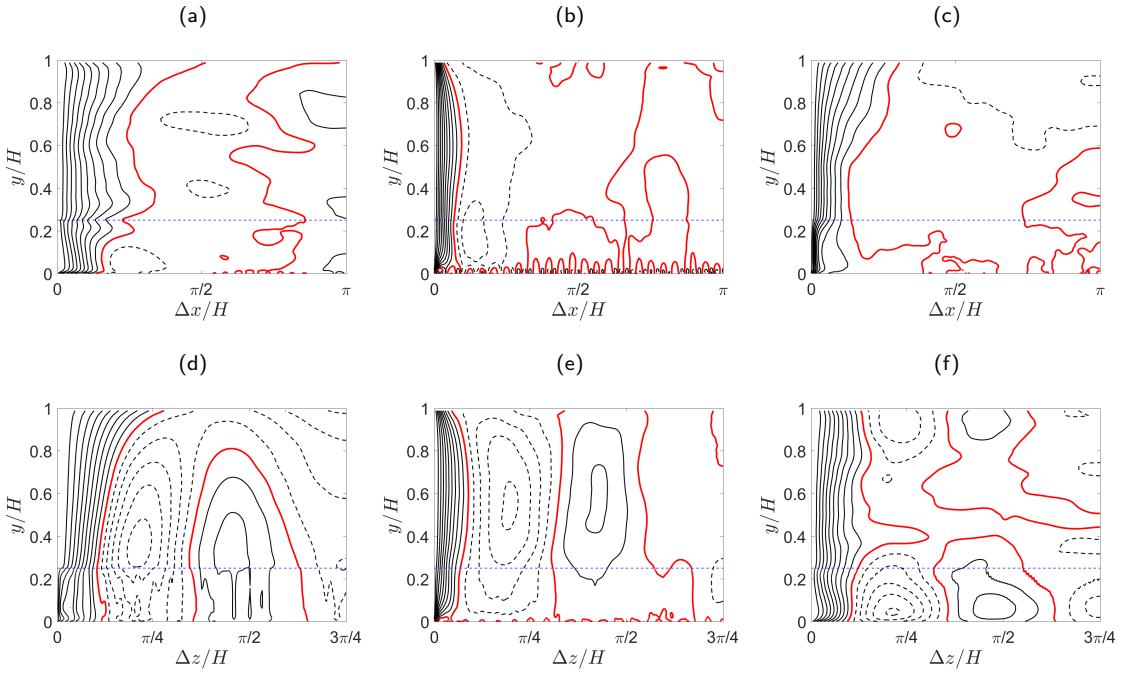

Figure 13: Contour maps showing the variation of the two-point autocorrelation functions of the velocity fluctuations in streamwise (top row panels) and spanwise (bottom row panels) directions. The contours are spaced by 0.1, starting from one. The negative values are plotted with a dashed line. The red line represents the zero-level. The leftmost column shows the streamwise velocity component $R_{u'u'}$, the central one shows the wall-normal component $R_{v'v'}$, and the rightmost column shows the spanwise component $R_{w'w'}$. Note that, in the panels of the first row, the spanwise average operator was pre-applied to the velocity fluctuations, and then the streamwise autocorrelation function was computed. In the panels of the second row, instead, the streamwise average operator was pre-applied to the velocity fluctuations, and then the spanwise autocorrelation function was computed (see equation (11) as an example).

eraging the u' and v' component) and by the instantaneous isocontours of the streamwise velocity components close to the bed, revealing a strong directional coherence albeit chopped by the sweep-ejection action of the outer quasi-streamwise vortices. Moreover, the appearance of spanwise oriented spanwise rollers is a ubiquitous characteristic of all flow fields over textured surfaces (e.g. canopies[29], porous[18] or ribletted walls[11]) that induce an inflection point in the mean velocity profile. In our case, the inflection point is generated by the discontinuous drag imposed by the canopy on the mean flow and is located at its tip. As already pointed out by Finnigan et al.[9], the inflection point leads to a Kelvin-Helmholtz instability that induces the formation of large spanwise rollers (Stuart's vortices) that are advected downstream by the mean flow. Finally, the panels (a) and (c) of Figure 14 show two intense peaks associated energy content of u' and w' fluctuations very close to the impermeable bed. These peaks are due to the presence of the wall that inhibits all wall-normal velocity fluctuations to take place. Because of the solenoidal condition on the flow field, strong accelerations or decelerations of the wall normal velocity imply an insurgence of

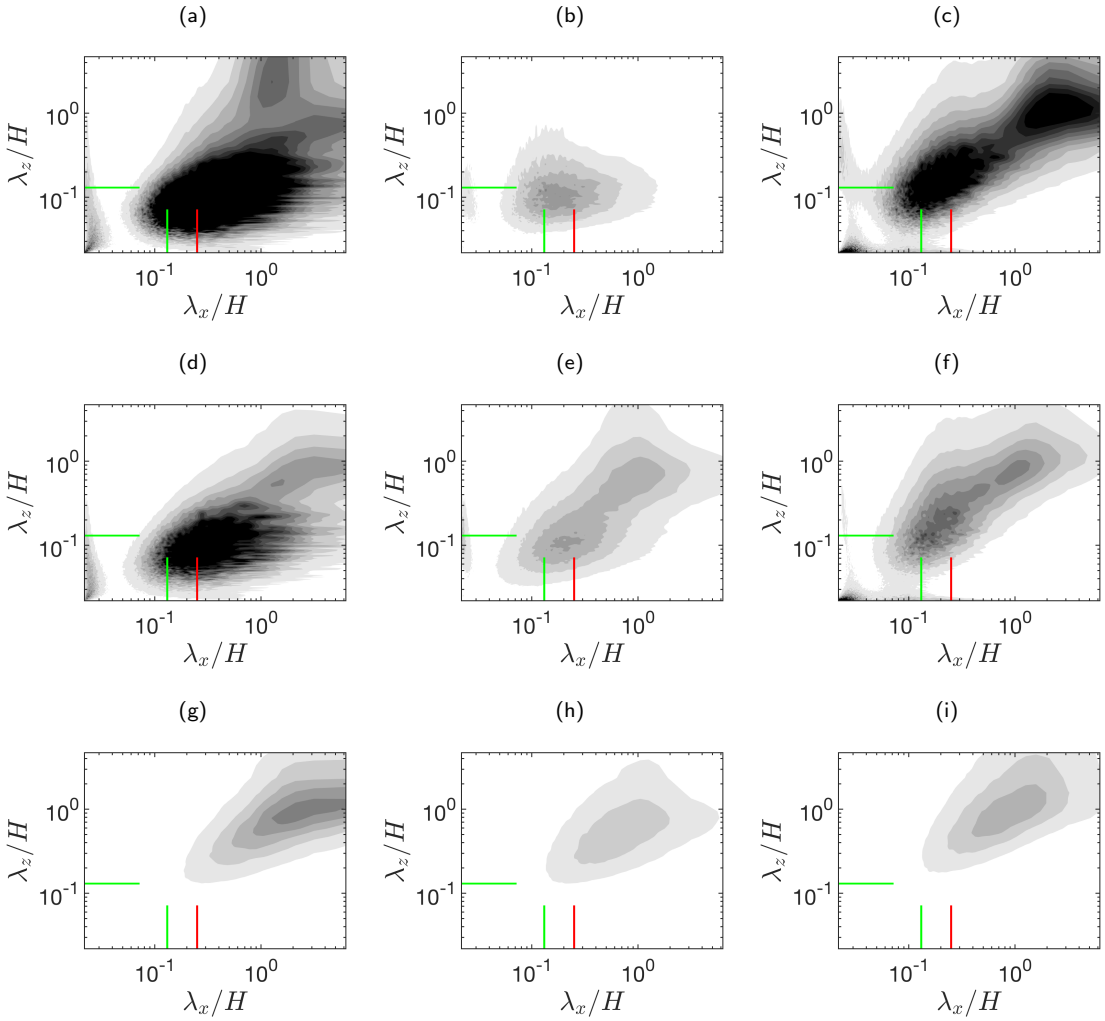

Figure 14: Contour maps showing the variation of the two-dimensional premultiplied velocity fluctuations spectra $\kappa_x\kappa_z\Phi_{u_i'u_i'}/u_{\tau,l}^2$ (u', v' and w' from left to right respectively), with wall-normal position $y/H = 0.02$ (first row from the top), $y/H = 0.18$ (second row from the top) and $y/H = 0.63$ (third row from the top). The short green lines mark the average filament spacing ΔS, while the short red line marks the filament height h. The darkest colour represents the highest value, the grey levels range from 0 to 0.1 with iso-levels sampled at each 0.01 interval.

in-plane motions (i.e. $\partial_y v = -(\partial_x u + \partial_z w)$). In particular, the sweeps and ejections induced by the outer quasi-streamwise vortices and the spanwise rollers generate coherent u' and w' patterns that are clearly visible in Figure 11.

IV. CONCLUSION

We have carried out a resolved numerical simulation of a turbulent flow over a rigid canopy with the aim of exploring the structure of the flow

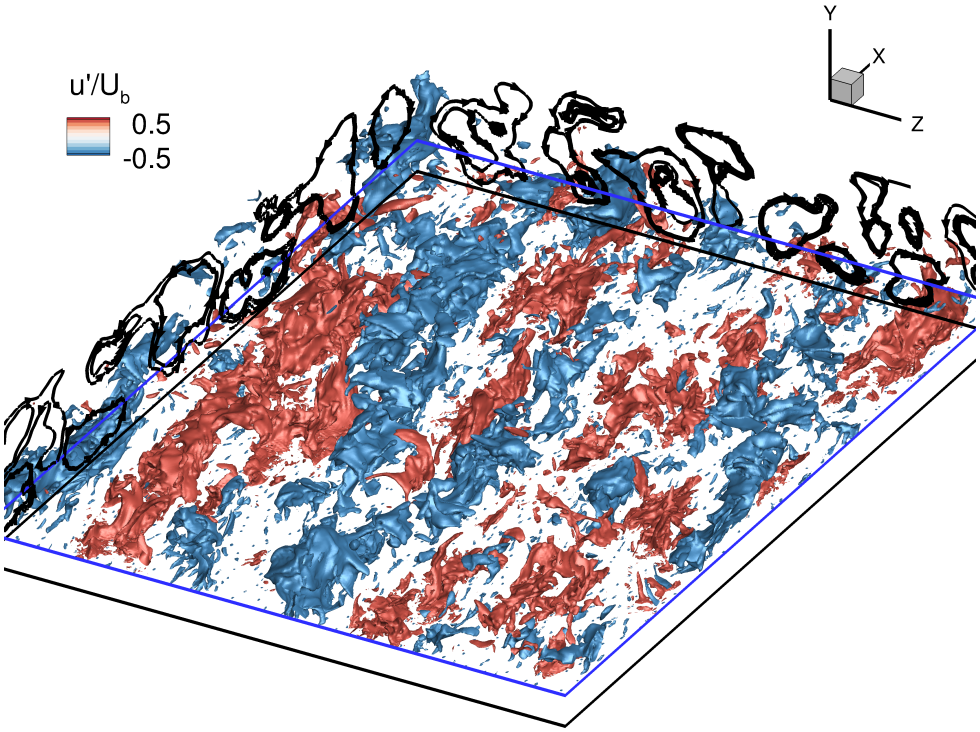

Figure 15: Instantaneous isosurfaces of streamwise velocity fluctuations. The streaklines drawn on the lateral sides have been obtained by averaging the instantaneous velocity fluctuations along the normal to the considered faces: the spanwise direction ($\langle u \rangle_z$, $\langle v \rangle_z$) for the left lateral side and the streamwise direction ($\langle v \rangle_x$,$\langle w \rangle_x$) for the frontal face.

generated by the interaction of a pressure-driven open-channel flow with a *mildly dense* filamentous layer covering the solid wall. This condition, often termed as *transitional*[29], is achieved when the ratio between the in-plane solidity and the depth of the canopy is fixed to a value that corresponds to a physical situation in which the outer, turbulent structures partially penetrate the canopy and the contribution to the total drag offered by the canopy itself is comparable in magnitude to the one generated by the shear at the bed.

The main conclusions of our work are of both methodological and physical character. Concerning the simulation methodology, it should be highlighted that the numerical technique that has been presented and validated in this work allows to carry out accurate and resolved canopy flow simulations efficiently. Indeed, to the authors' knowledge, this is the first time that a canopy-flow simulation in which the physical boundary values are imposed stem-by-stem has been reported in the literature.

The other main conclusions concern the physical characterisation of the flow. In the particular regime that has been considered the flow can be roughly divided into three regions. The outer region shows strong similarities with high Reynolds number wall turbulence developing over a rough, solid boundary. The classical logarithmic velocity

profile can be obtained by introducing a classical shift of the origin of the wall-normal axis (i.e. a *virtual origin* located inside the canopy). The scalings of the outer fluctuations, normalised in wall units based on the friction velocity obtained from the total stress at the virtual origin, also present a reasonable collapse over data obtained by other authors in the logarithmic layer of turbulent channel flows at moderately high Reynolds numbers. The structure of the outer flow resembles the one found within the logarithmic layer of wall-flows at Reynolds numbers sufficiently high to allow a scale separation: long elongated velocity streaks flanked by vortices oriented along the streamwise direction. The streamwise vortices are particularly intense and, because of the high wall-normal permeability of the canopy, penetrate the full canopy, down to until reaching the bed. The intra-canopy-region velocity distribution scales reasonably well with a friction velocity distribution obtained locally along the wall-normal direction.

The mean velocity profile shows two inflections points. The top one is imposed at the canopy tip by the drag discontinuity and, in turns, it is known to trigger a Kelvin-Helmholtz instability producing a series of counter-rotating spanwise rollers that may form a mixing layer of constant thickness above the canopy[29]. According to some authors, this system of spanwise vortices would induce a series of alternating regions of upwash and downwash events that would locally bend up or bend down the rollers forming the so-termed *head-up*, *head-down* hairpin vortices[9]. Our simulation seems to offer an alternative point of view in which the spanwise vorticity formed as a consequence of the inflectional instability loose part of its coherence as a result of the strong sweeps and ejections generated by the outer, quasi-streamwise vortices. The existence or the prevalence of this mechanism or of the one based on the self-induced lifting and depression of the rollers proposed by other authors probably depends on the parameter defining the canopy solidity and their exploration is underway.

Finally, the region in the proximity of the bed is again strongly influenced by the outer structures which provoke vigorous inrush and ejections towards and from the bed that encounter almost no resistance in the wall-normal direction. The wall-normal velocity field induced by the outer flow interact with the impermeable bed conditions forming organised streamwise and spanwise velocity patterns in the proximity of the wall.

REFERENCES

[1]Bailey, B. and Stoll, R. (2013). Turbulence in sparse, organized vegetative canopies: a large-eddy simulation study. *Boundary-Layer Meteorology*, 147(3):369–400.

[2]Bailey, B. and Stoll, R. (2016). The creation and evolution of coherent structures in plant canopy flows and their role in turbulent transport. *Journal of Fluid Mechanics*, 789:425–460.

[3]Balay, S., Abhyankar, S., Adams, M. F., Brown, J., Brune, P., Buschelman, K., Dalcin, L., Eijkhout, V., Gropp, W. D., Kaushik, D., Knepley, M. G., May, D. A., McInnes, L. C., Rupp, K., Smith, B. F., Zampini, S., Zhang, H., and Zhang, H. (2017). PETSc Web page. `http://www.mcs.anl.gov/petsc`.

[4]Belcher, S., Jerram, N., and Hunt, J. (2003). Adjustment of a turbulent boundary layer to a canopy of roughness elements. *Journal of Fluid Mechanics*, 488:369–398.

[5]Cui, J. and Neary, V. (2008). Les study of turbulent flows with submerged vegetation. *Journal of Hydraulic Research*, 46(3):307–316.

[6]Fadlun, E., Verzicco, R., Orlandi, P., and Mohd-Yusof, J. (2000). Combined immersed-boundary finite-difference methods for three-dimensional complex flow simulations. *Journal of Computational Physics*, 161(1):35–60.

[7]Favier, J., Revell, A., and Pinelli, A. (2014). A lattice boltzmann–immersed boundary method to simulate the fluid interaction with moving and slender flexible objects. *Journal of Computational Physics*, 261:145–161.

[8]Finnigan, J. (2000). Turbulence in plant canopies. *Annual Review of Fluid Mechanics*, 32(1):519–571.

[9]Finnigan, J., Shaw, R., and Patton, E. (2009). Turbulence structure above a vegetation canopy. *Journal of Fluid Mechanics*, 637:387–424.

[10]Flores, O. and Jiménez, J. (2006). Effect of wall-boundary disturbances on turbulent channel flows. *Journal of Fluid Mechanics*, 566:357–376.

[11]García-Mayoral, R. and Jiménez, J. (2011). Hydrodynamic stability and breakdown of the viscous regime over riblets. *Journal of Fluid Mechanics*, 678:317–347.

[12]Ghisalberti, M. and Nepf, H. (2002). Mixing layers and coherent structures in vegetated aquatic flows. *Journal of Geophysical Research: Oceans*, 107(C2).

[13]Ghisalberti, M. and Nepf, H. (2004). The limited growth of vegetated shear layers. *Water Resources Research*, 40(7).

[14]Harman, I. N. and Finnigan, J. J. (2007). A simple unified theory for flow in the canopy and roughness sublayer. *Boundary-layer meteorology*, 123(2):339–363.

[15]Hoyas, S. and Jiménez, J. (2008). Reynolds number ef-

fects on the reynolds-stress budgets in turbulent channels. *Physics of Fluids*, 20(10):101511.

[16]Huang, J., Cassiani, M., and Albertson, J. (2009). The effects of vegetation density on coherent turbulent structures within the canopy sublayer: a large-eddy simulation study. *Boundary-Layer Meteorology*, 133(2):253–275.

[17]Jiménez, J. (2004). Turbulent flows over rough walls. *Annu. Rev. Fluid Mech.*, 36:173–196.

[18]Jiménez, J., Uhlmann, M., Pinelli, A., and Kawahara, G. (2001). Turbulent shear flow over active and passive porous surfaces. *Journal of Fluid Mechanics*, 442:89–117.

[19]Kim, J. and Moin, P. (1985). Application of a fractional-step method to incompressible navier-stokes equations. *Journal of Computational Physics*, 59(2):308–323.

[20]Kim, J., Moin, P., and Moser, R. (1987). Turbulence statistics in fully developed channel flow at low reynolds number. *Journal of fluid mechanics*, 177:133–166.

[21]Leonard, A. (1975). Energy cascade in large-eddy simulations of turbulent fluid flows. *Advances in Geophysics*, 18:237–248.

[22]Lightbody, A. and Nepf, H. (2006). Prediction of velocity profiles and longitudinal dispersion in salt marsh vegetation. *Limnology and Oceanography*, 51(1):218–228.

[23]Liu, D., Diplas, P., Fairbanks, J., and Hodges, C. (2008). An experimental study of flow through rigid vegetation. *Journal of Geophysical Research: Earth Surface*, 113(F4).

[24]López, F. and García, M. (2001). Mean flow and turbulence structure of open-channel flow through non-emergent vegetation. *Journal of Hydraulic Engineering*, 127(5):392–402.

[25]Luhar, M., Rominger, J., and Nepf, H. (2008). Interaction between flow, transport and vegetation spatial structure. *Environmental Fluid Mechanics*, 8(5-6):423.

[26]Mars, R., Mathew, K., and Ho, G. (1999). The role of the submergent macrophyte triglochin huegelii in domestic greywater treatment. *Ecological Engineering*, 12(1):57–66.

[27]Mizuno, Y. and Jiménez, J. (2013). Wall turbulence without walls. *Journal of Fluid Mechanics*, 723:429–455.

[28]Neary, V., Constantinescu, S., Bennett, S., and Diplas, P. (2011). Effects of vegetation on turbulence, sediment transport, and stream morphology. *Journal of Hydraulic Engineering*, 138(9):765–776.

[29]Nepf, H. (2012). Flow and transport in regions with aquatic vegetation. *Annual Review of Fluid Mechanics*, 44:123–142.

[30]Nepf, H. and Vivoni, E. (2000). Flow structure in depth-limited, vegetated flow. *Journal of Geophysical Research: Oceans*, 105(C12):28547–28557.

[31]Nezu, I. and Sanjou, M. (2008). Turburence structure and coherent motion in vegetated canopy open-channel flows. *Journal of Hydro-Environment Research*, 2(2):62–90.

[32]Omidyeganeh, M. and Piomelli, U. (2011). Large-eddy simulation of two-dimensional dunes in a steady, unidirectional flow. *Journal of Turbulence*, (12):N42.

[33]Omidyeganeh, M. and Piomelli, U. (2013a). Large-eddy simulation of three-dimensional dunes in a steady, unidirectional flow. part 1. turbulence statistics. *Journal of Fluid Mechanics*, 721:454–483.

[34]Omidyeganeh, M. and Piomelli, U. (2013b). Large-eddy simulation of three-dimensional dunes in a steady, unidirectional flow. part 2. flow structures. *Journal of Fluid Mechanics*, 734:509–534.

[35]Pinelli, A., Naqavi, I., Piomelli, U., and Favier, J. (2010). Immersed-boundary methods for general finite-difference and finite-volume navier–stokes solvers. *Journal of Computational Physics*, 229(24):9073–9091.

[36]Poggi, D., Porporato, A., Ridolfi, L., Albertson, J., and Katul, G. (2004). The effect of vegetation density on canopy sub-layer turbulence. *Boundary-Layer Meteorology*, 111(3):565–587.

[37]Raupach, M., Finnigan, J., and Brunei, Y. (1996). Coherent eddies and turbulence in vegetation canopies: the mixing-layer analogy. *Boundary-Layer Meteorology*, 78(3-4):351–382.

[38]Ree, W. and Palmer, V. (1949). *Flow of water in channels protected by vegetative linings*. Number 967. US Dept. of Agriculture.

[39]Rhie, C. and Chow, W. (1983). Numerical study of the turbulent flow past an airfoil with trailing edge separation. *AIAA Journal*, 21(11):1525–1532.

[40]Rosti, M. E., Omidyeganeh, M., and Pinelli, A. (2016). Direct numerical simulation of the flow around an aerofoil in ramp-up motion. *Physics of Fluids*, 28(2):025106.

[41]Rouhi, A., Piomelli, U., and Geurts, B. J. (2016). Dynamic subfilter-scale stress model for large-eddy simulations. *Physical Review Fluids*, 1(4):044401.

[42]Scotti, A. (2006). Direct numerical simulation of turbulent channel flows with boundary roughened with virtual sandpaper. *Physics of Fluids*, 18(3):031701.

[43]Sharma, A. and García-Mayoral, R. (2018). Turbulent flows over sparse canopies. In *Journal of Physics: Conference Series*, volume 1001, page 012012. IOP Publishing.

[44]Shimizu, Y., Tsujimoto, T., Nakagawa, H., and Kitamura, T. (1991). Experimental study on flow over rigid vegetation simulated by cylinders with equi-spacing. *Doboku Gakkai Ronbunshu*, 1991(438):31–40.

[45]Tuerke, F. and Jiménez, J. (2013). Simulations of turbulent channels with prescribed velocity profiles. *Journal of Fluid Mechanics*, 723:587–603.

[46]Watanabe, T. (2004). Large-eddy simulation of coherent turbulence structures associated with scalar ramps over plant canopies. *Boundary-Layer Meteorology*, 112(2):307–341.

[47]Wilcock, R., Champion, P., Nagels, J., and Croker, G. (1999). The influence of aquatic macrophytes on the hydraulic and physico-chemical properties of a new zealand lowland stream. *Hydrobiologia*, 416:203–214.

[48]Yang, U. M. et al. (2002). Boomeramg: a parallel algebraic multigrid solver and preconditioner. *Applied Numerical Mathematics*, 41(1):155–177.